Journal of *Marine Science and Engineering*

MDPI

Article

Underwater Target Localization Method Based on Uniform Linear Electrode Array

Wenjing Shang [1], Feixiang Gao [1], Jiahui Liu [2], Yunhe Pang [3], Sergey V. Volvenko [4], Vladimir M. Olshanskiy [5] and Yidong Xu [3,*]

[1] School of Physics and Electronic Information, Yantai University, Yantai 264005, China; shangwenjing@ytu.edu.cn (W.S.); 202400357046@s.ytu.edu.cn (F.G.)
[2] College of Information and Communication Engineering, Harbin Engineering University, Harbin 150001, China; liujh@hrbeu.edu.cn
[3] Yantai Research Institute, Harbin Engineering University, Yantai 264006, China; pyhytu@163.com
[4] Higher School of Applied Physics and Space Technologies, Peter the Great St. Petersburg Polytechnic University (SPbPU), 195251 St. Petersburg, Russia; volk@cee.spbstu.ru
[5] A.N. Severtsov Institute of Ecology and Evolution, Russian Academy of Sciences, 119071 Moscow, Russia; vmolsh@yandex.ru
* Correspondence: xuyidong@hrbeu.edu.cn; Tel.: +86-132-6350-7375

Abstract: The underwater electric field signal can be excited by underwater vehicles, such as the shaft-rate electric field and the corrosion electric field. The electric field signature of each vehicle exhibits significant differences in time and frequency domain, which can be exploited to determine target positions. In this paper, a novel passive localization method for underwater targets is presented, leveraging a uniform linear electrode array (ULEA). The ULEA manifold along the axial direction is derived from the electric field propagation in an infinite lossy medium, which provides the nonlinear mapping relationship between the target position and the voltage data acquired by the ULEA. In order to locate the targets, the multiple signal classification (MUSIC) algorithm is applied. Then, capitalizing on the rotational invariance of matrix operations and exploiting the symmetry inherent in the ULEA, we streamline the six-dimensional spatial spectral scanning onto a two-dimensional plane, providing azimuth and distance information for the targets. This method significantly reduces computational overhead. To validate the efficacy of our proposed method, we devise a localization system and conduct a simulation environment to estimate targets. Results show that our method achieves satisfactory direction and reliable distance estimations, even in scenarios with low signal-to-noise ratios.

Keywords: underwater electric field sources; target locating; uniform linear electrode array

Academic Editor: Pasqualino Corigliano

Received: 6 January 2025
Revised: 29 January 2025
Accepted: 5 February 2025
Published: 6 February 2025

Citation: Shang, W.; Gao, F.; Liu, J.; Pang, Y.; Volvenko, S.V.; Olshanskiy, V.M.; Xu, Y. Underwater Target Localization Method Based on Uniform Linear Electrode Array. *J. Mar. Sci. Eng.* **2025**, *13*, 306. https://doi.org/10.3390/jmse13020306

1. Introduction

The determination of the source position constitutes a crucial aspect of target parameter estimation. Within the realm of marine engineering, underwater electric field source localization technology offers distinct advantages, including stable signal transmission, rapid propagation speed, and relatively simple equipment, distinguishing it from other positioning methodologies [1,2]. Consequently, it finds wide-ranging applications, including subsea cable detection [3], underwater obstacle avoidance [4], underwater pre-touch [5], ship navigation [6], and cooperative positioning of underwater vehicles [7,8]. Nonetheless, the electric field experiences rapid attenuation with increasing propagation distance in an underwater medium. Consequently, there is a pressing need for effective methods to enhance the precision in the estimation of electric field source location.

In recent years, various methods have been proposed for the localization of underwater electric field sources. These include the integration of radar signal processing techniques [4,9–12], electrode array-based methodologies [13–15], neural network-driven approaches [16,17], and active electric field frequency domain-based methods [18–21]. In addition to addressing the localization of stationary objects, some scholars have focused on the underwater detection of moving objects [22–24]. Zhang et al. [4] introduced a TLS-ESPRIT-based azimuth estimation algorithm that derives parameter estimates through the processing of Poynting vectors, without requiring prior frequency information and eliminating frequency ambiguity. Lim et al. [10] proposed a generalized multiple signal classification (MUSIC) algorithm adaptable to different underwater noise forms, adjusting stability through parameter manipulation based on distinct noise covariance matrices. Shang et al. [12] introduced an improved underwater electric field-based target localization algorithm, which combines a subspace scanning algorithm and meta-EP PSO. In this algorithm, the uniform circular electrodes were used to detect a dipole source. Yang et al. [13] introduced a multiscale sparse array of electromagnetic vector sensors, measuring electric and magnetic field components simultaneously, along with a multiscale disambiguation algorithm for highly accurate direction of arrival (DOA) estimation of multiple signal sources. Wang et al. [16] proposed a localization method that combines passive electric and magnetic fields. Electromagnetic sensor arrays collected sample data, which underwent pre-processing before a back propagation (BP) neural network modeled the electric dipole source's electromagnetic field distribution, yielding accurate localization results. Peng's work [18] involved building a finite element model (FEM) for an active electrolocation system in underwater environments, employing the coupling Cole–Cole model and Maxwell's theory. Ren et al. [20] proposed an amplitude-informed frequency characteristic (AIFC) identification algorithm for underwater active electric field localization, utilizing multi-frequency excitation signals to significantly enhance localization efficiency compared to traditional single-frequency excitation methods. Li et al. [24] introduced a novel tracking strategy for a moving dipole. The projection approximation subspace tracking (PAST) method, based on a subspace update, was employed for initial tracking estimates, followed by Kalman filtering (KF) to optimize trajectory estimation and improve tracking accuracy.

Continuous advancements in ocean exploration and the increasing complexity of the marine environment underscore the need for enhanced efficiency and applicability in underwater electric field source azimuth and distance estimation. Drawing inspiration from array signal processing techniques, this paper proposes the design of a uniform linear electrode array (ULEA) for passive electric field source localization. The corresponding array manifold along the axis direction is derived, which establishes the mapping relationship between the target parameters (the distance, azimuth, zenith, and source direction) and the voltage data acquired by the ULEA. To reduce the computation burden of the 6-D spatial, the rotation-invariant feature of the ULEA manifold is utilized, thereby providing 2-D spatial, which significantly simplifies the operation. Target location performance and resolution are also studied for given ULEA structures.

The main contributions of this paper are: (1) a method of passive electric field source localization based on ULEA and (2) simplification of the calculation of the spatial spectral complexity and the direction of polarization of the signal source. The rest of this paper is organized as follows. In Section 2, the mathematical expression of the ULEA array manifold is derived from the electric dipole model in an infinite homogeneous medium. Then, the rotational invariance of matrix operations and the symmetry of ULEA are utilized to reduce the computational spatial spectral complexity in the MUSIC algorithm. The simulations are presented in Section 3. In Section 4, simulation results demonstrate that the proposed method achieves high accuracy in azimuth estimation and can provide reference

in target source distance estimation. The effects of ULEA structure and array manifold on localization accuracy are also discussed in this section. Conclusions and possible directions of future work are given in Section 5.

2. MUSIC Method

2.1. Locating System

This paper aims to determine the 2D spatial coordinates of electric sources in a water environment by using the ULEA. Sacrificial anode protection, which prevents seawater corrosion, is a key measure to protect ships during long-term sailing. This protection system generates an electric field in saltwater, which can inadvertently expose the ship's position. Additionally, the shaft-rate electric field is another source of exposure for ships, which contains distinctive features of the ship, such as the rotary speed, harmonic frequency of the engine, etc. [25]. The ships' shaft-rate electric fields are orthogonal to each other over the long term as the engine power constitutes independent events. Based on this property, we propose a 2D electric source localization method using multiple signal classification.

Consider a ULEA of $M = 2L + 1$ electric sensors as shown in Figure 1, which are ranged along the x-axis. The center of the ULEA is located at the origin of the coordinate O and the distance between each electric sensor is Δl. Thus, the position of the kth electric sensor $\mathbf{r}_k^a$ is $(k\Delta l, 0, 0)^{\mathrm{T}}$, where $k = -L, -L+1, \cdots, 0, \cdots, L-1, L$, and T is the transposition. The 0th electric sensor at the center of the ULEA is defined as the reference sensor.

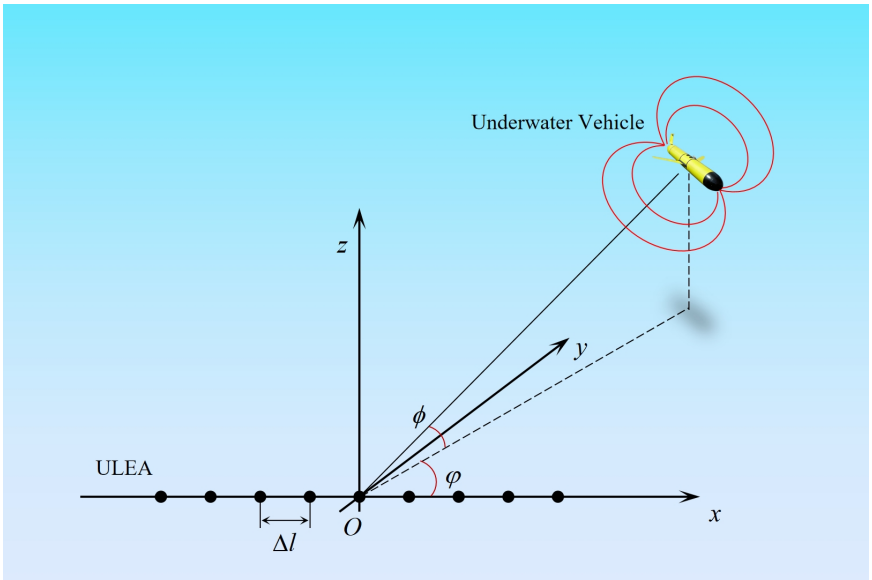

Figure 1. ULEA vector rotate model, where the vectors $\mathbf{e}_p$ and $\mathbf{e}_{r_k}$ are rotated ϕ along the x-axis.

Generally, the ship target that we are locating can be seen as a dipole when the distance from the target to the ULEA being much greater than the ship size. Assuming an electric dipole source being placed at point P, the distance from P to coordinate origin O is r_0 (in m). The electric dipole source azimuth in the horizontal plane ($x - y$ plane) is φ and the zenith angle is ϕ. Thus, the vector from the electric dipole source to the kth electric sensor $\mathbf{r}_k$ is given

$$\mathbf{r}_k = \mathbf{r}_k^a - r_0 \begin{pmatrix} \cos\phi\cos\varphi \\ \cos\phi\sin\varphi \\ \sin\phi \end{pmatrix}. \tag{1}$$

Furthermore, the source dipole moment is $\mathbf{p} = p(t)\mathbf{e}_p$, where $p(t)$ is the signal intensity in time domain and $\mathbf{e}_p$ is the direction vector.

Based on the electric field propagation in infinite lossy medium [26]. The field received at the kth ULEA sensor can be derived:

$$\mathbf{E}_k = \frac{p(t)}{4\pi\sigma}\frac{e^{-\beta r_k}}{r_k^3}\begin{Bmatrix} 2(\mathbf{e}_p^{\mathrm{T}}\mathbf{e}_{r_k})\mathbf{e}_{r_k}(1+\beta r_k + j\beta r_k) \\ +(\mathbf{e}_p \times \mathbf{e}_{r_k}) \times \mathbf{e}_{r_k}\left[1+\beta r_k + j(\beta r_k + 2\beta^2 r_k^2)\right] \end{Bmatrix} e^{-j\beta r_k} e^{j\omega t}, \tag{2}$$

where $\mathbf{e}_{r_k}$ is the direction vector from the source target to the kth ULEA sensor, $r_k = |\mathbf{r}_k|$ represents the distance between the source target and the kth sensor, and σ is the conductivity of water (in S/m), β is the phase constant. For highly lossy water media, the phase constant can be approximated as $\beta \approx \sqrt{\frac{\omega\mu\sigma}{2}}$, where ω is the signal angular frequency (in rad/s) and μ is the magnetic permeability of water (in H/m).

In order to simplify the calculation, we replace the variables based on Equation (2), according to the functionality of the parameters. We have $\eta = \frac{p(t)}{4\pi\sigma}e^{j\omega t}$, which is only related to the source strength. The spatial attenuation factor is given $g_k = \frac{e^{-\beta r_k}}{r_k^3}$. The direction vectors from the electric source to the ULEA sensor are $\mathbf{w}_{1k} = 2(\mathbf{e}_p^{\mathrm{T}}\mathbf{e}_{r_k})\mathbf{e}_{r_k}$, $\mathbf{w}_{2k} = (\mathbf{e}_p \times \mathbf{e}_{r_k}) \times \mathbf{e}_{r_k}$, respectively. The corresponding phase factors are $y_{1k} = 1 + \beta r_k + j\beta r_k$ and $y_{2k} = 1 + \beta r_k + j(\beta r_k + 2\beta^2 r_k^2)$. For a practical locating system, the acquired signal is the voltage between two electrodes of the ULEA sensors, not the electric field with three direction components. As the ULEA along the x-axis, we get the x-axis direction signal. Thus, the $\mathbf{e}_x$ components of $\mathbf{w}_{1k}$ and $\mathbf{w}_{2k}$ are obtained with $w_{1k}^x = \mathbf{e}_x^{\mathrm{T}}\mathbf{w}_{1k}$, $w_{2k}^x = \mathbf{e}_x^{\mathrm{T}}\mathbf{w}_{2k}$.

Generally, the electrode's interval l_δ of each ULEA voltage sensor can be seen as small enough that the electric field is uniformly distributed between two adjacent electrodes. Thus, the instantaneous signal voltage of the kth sensor received is expressed as follows:

$$u_k = \xi_k \mathbf{W}_k^{\mathrm{T}} \mathbf{Y}_k e^{-j\beta\Delta d_k} s(t), \tag{3}$$

where $\mathbf{W}_k = \left[w_{1k}^x \; w_{2k}^x\right]^{\mathrm{T}}$, $\mathbf{Y}_k = \left[y_{1k} \; y_{2k}\right]^{\mathrm{T}}$. Δd_k is the relative distance, which is given $\Delta d_k = r_k - r_0$. The term $s(t)$ is a function about the signal attenuation in the propagation route, which can be written as $s(t) = l_\delta \eta g_0 e^{-j\beta r_0}$. The corresponding relative spatial attenuation factor is given by $\xi_k = \frac{g_k}{g_0}$. Equation (3) represents the forward model, which indicates that if prior information about the source is available, such as the signal strength $p(t)$, spatial coordinates $(\varphi,\ \phi,\ r_0)$ and the dipole moment direction $\mathbf{e}_p$, then the ULEA sensor voltage can be determined. This forms the basis for constructing the position array manifold in the following section.

2.2. Array Manifold

In a practical situation, the signal $s(t)$ is sampled at a fixed frequency by an analog-to-digital converter (ADC), yielding discrete time serial $\mathbf{s}$, which is a $1 \times T$ matrix. Thus, based on Equation (3), the signal matrix $\mathbf{X}$ of the ULEA can be expressed as

$$\mathbf{X} = \mathbf{a}\mathbf{s}, \tag{4}$$

where $\mathbf{a}$ is the array manifold, which contains all the spatial coordinates information of the electric source with a size of $M \times 1$. Moreover, different from the canonical DOA algorithm like radar application (it estimates the target azimuth in 1-D space), the array manifold contains 6 parameters $\mathbf{a}(\varphi,\ \phi,\ r_0,\ \mathbf{e}_p)$, which compose a 6-D space. Thus, $\mathbf{X}$ is a matrix of size $M \times T$. The expansion of $\mathbf{a}$ is as follows:

$$\mathbf{a} = \begin{bmatrix} \xi_{-L}\mathbf{W}_{-L}^{\mathrm{T}}\mathbf{Y}_{-L}e^{-j\beta\Delta d_{-L}} \\ \vdots \\ \mathbf{W}_{0}^{\mathrm{T}}\mathbf{Y}_{0} \\ \xi_{1}\mathbf{W}_{1}^{\mathrm{T}}\mathbf{Y}_{1}e^{-j\beta\Delta d_{1}} \\ \vdots \\ \xi_{L}\mathbf{W}_{L}^{\mathrm{T}}\mathbf{Y}_{L}e^{-j\beta\Delta d_{L}} \end{bmatrix}. \tag{5}$$

In fact, there is more than one vessel to be located at the same time. Suppose the number of electric sources is D, where $D < M$. They are located at point $(\varphi_1,\ \phi_1,\ r_{01})$, $(\varphi_2,\ \phi_2,\ r_{02}), \cdots, (\varphi_D,\ \phi_D,\ r_{0D})$, corresponding with the signals $\mathbf{S} = [\mathbf{s}_1\ \ \mathbf{s}_2\ \ \cdots\ \ \mathbf{s}_D]^{\mathrm{T}}$, assuming that the incident signals are uncorrelated. According to Equation (5), we can obtain array manifold of each electric source, yielding $\mathbf{A} = [\mathbf{a}_1\ \mathbf{a}_2\ \cdots\ \mathbf{a}_D]$ with size of $M \times D$. Moreover, the signal received by the ULEA is corrupted by noise, which typically includes atmospheric interference, electrochemical noise, and system thermal noise. We assume that the signal is mixed with additive white Gaussian noise (AWGN) $\mathbf{N}$, which is zero mean with the covariance of $E\{\mathbf{N}\mathbf{N}^{\mathrm{T}}\} = \sigma_N^2\mathbf{I}$, where $E\{\cdot\}$ denotes the expected value of the argument and $\mathbf{I}$ is identity matrix. For several electric source's location, the Equation (4) can be rewritten as

$$\mathbf{X} = \mathbf{A}\mathbf{S} + \mathbf{N}. \tag{6}$$

2.3. Spatial Spectrum

When signals and noise are uncorrelated, the ensemble averaged covariance matrix of $\mathbf{X}$ in Equation (6) can be expressed as

$$\mathbf{R} = E\left[\mathbf{X}\mathbf{X}^{\mathrm{H}}\right] = \frac{1}{T}\mathbf{X}\mathbf{X}^{\mathrm{H}} = \mathbf{A}\mathbf{Q}\mathbf{A}^{\mathrm{H}} + \sigma_N^2\mathbf{I} = \sum_{i=1}^{M}\lambda_i\mathbf{v}_i\mathbf{v}_i^H = \mathbf{V}\mathbf{\Lambda}\mathbf{V}^{\mathrm{H}}. \tag{7}$$

Here, superscript H represents the conjugate transpose; $\mathbf{Q}$ is a $D \times D$ diagonal matrix with the incident signal powers on the diagonal, which is given by $\mathbf{Q} = E\{\mathbf{S}\mathbf{S}^{\mathrm{H}}\}$. λ_i represents the eigenvalue of $\mathbf{R}$, arranged as $\lambda_1 \geq \lambda_2 \geq \cdots \geq \lambda_M$. $\mathbf{v}_i$ denotes the eigenvector corresponding to λ_i. $\mathbf{\Lambda}$ is a diagonal matrix with the eigenvalues λ_i, which can be expressed as $\mathbf{\Lambda} = diag(\lambda_1,\ \lambda_2,\ \cdots,\ \lambda_M)$. Meanwhile, $\mathbf{V}$ is composed of the corresponding eigenvectors, which is $\mathbf{V} = [\mathbf{v}_1\ \mathbf{v}_2\ \cdots\ \mathbf{v}_M]$.

According to the standard MUSIC algorithm, the matrix $\mathbf{V}$ is formed by the signal and noise subspace, which is given by $\mathbf{V} = [\mathbf{V}_S\ \mathbf{V}_N]$. The signal subspace $\mathbf{V}_S$ is spanned by the first D eigenvectors, yielding $\mathbf{V}_S = [\mathbf{v}_1\ \mathbf{v}_2\ \cdots\ \mathbf{v}_D]$. It indicates that the array manifold $\mathbf{a}_1,\ \mathbf{a}_2,\ \cdots,\ \mathbf{a}_D$ are linear combinations of the eigenvectors in signal subspace. The span of the last $M - D$ eigenvectors compose the noise subspace $\mathbf{V}_N = [\mathbf{v}_{D+1}\ \cdots\ \mathbf{v}_M]$.

The projection matrix onto the noise subspace can be derived

$$\mathbf{P}_N = \mathbf{V}_N\mathbf{V}_N^{\mathrm{H}}. \tag{8}$$

The spatial spectrum of the standard MUSIC-like algorithm is then given by

$$P(\varphi,\ \phi,\ r_0,\ \mathbf{e}_p) = \frac{1}{\mathbf{a}^{\mathrm{H}}\mathbf{P}_N\mathbf{a}}. \tag{9}$$

It is shown in Equation (9) that the spatial spectrum is in 6-D space. It will introduce a heavy computation overhead on traversing all the parameter points in a limited 6-D space. For example, suppose the azimuth $\varphi \in (30^\circ,\ 150^\circ)$, with the angular sampling interval $\pi/150$, yielding 100 sample points; let the zenith ϕ be within the interval $(30^\circ,\ 150^\circ)$,

with the angular sampling interval $\pi/150$, yielding 100 sample points; the distance r_0 from the electric source to the ULEA is within $(30,\ 330)$, and the distance interval is 10 m, providing 30 points. Furthermore, the number of electric source dipole moment steering vector sample points is 10 for each direction axis. Therefore, the spatial spectrum points that the locating system calculates for finding maximum values would be 3×10^8, which is intolerable for underwater energy-limited monitor stations. Thus, we have to optimize the locating algorithm to reduce the calculation.

2.4. Reducing the Calculation

In this section, we propose the reducing calculation method based on the ULEA's symmetry about the x-axis. Suppose two vectors are in the coordinate system namely, $\mathbf{b}$, $\mathbf{c}$, which are rotated θ along the x-axis, yielding vectors $\mathbf{b}'$ and $\mathbf{c}'$, respectively. As a result, the rotation matrix $\mathbf{R}_x$ can be expressed as

$$\mathbf{R}_x = \begin{bmatrix} 1 & 0 & 0 \\ 0 & \cos\theta & -\sin\theta \\ 0 & \sin\theta & \cos\theta \end{bmatrix}. \tag{10}$$

Thus, we have $\mathbf{b}' = \mathbf{R}_x\mathbf{b}$ and $\mathbf{c}' = \mathbf{R}_x\mathbf{c}$. Meanwhile, the cross productions $\mathbf{h}$ and $\mathbf{h}'$ are given by $\mathbf{h} = \mathbf{b} \times \mathbf{c}$ and $\mathbf{h}' = \mathbf{b}' \times \mathbf{c}'$, respectively. In order to simplify the derivation, the cross production operator can be transformed to a matrix type, which is given

$$\mathbf{b}\times = \begin{bmatrix} 0 & -b_z & b_y \\ b_z & 0 & -b_x \\ -b_y & b_x & 0 \end{bmatrix} = \mathbf{B}. \tag{11}$$

Similarly, we also have $\mathbf{c}\times = \mathbf{C}$, $\mathbf{b}'\times = \mathbf{B}'$ and $\mathbf{c}'\times = \mathbf{C}'$. Then, the rotation can be expressed as

$$\mathbf{h}' = \mathbf{R}_x\mathbf{h} = \mathbf{R}_x(\mathbf{b} \times \mathbf{c}) = \mathbf{R}_x\mathbf{B}\mathbf{c} = \mathbf{B}'\mathbf{c}' = \mathbf{B}'\mathbf{R}_x\mathbf{c}. \tag{12}$$

According to Equation (12), it can be noted that $\mathbf{R}_x\mathbf{B}\mathbf{c} = \mathbf{B}'\mathbf{R}_x\mathbf{c}$ for arbitrary vector $\mathbf{c}$, which means $\mathbf{R}_x\mathbf{B} = \mathbf{B}'\mathbf{R}_x$. Then, we can obtain $\mathbf{B}' = \mathbf{R}_x\mathbf{B}\mathbf{R}_x^{\mathrm{T}}$. Furthermore, the x-axis component of the cross production can be derived as follows

$$\mathbf{e}_x^{\mathrm{T}}\left[(\mathbf{b}' \times \mathbf{c}') \times \mathbf{c}'\right] = -\mathbf{e}_x^{\mathrm{T}}\mathbf{R}_x\mathbf{C}\mathbf{R}_x^{\mathrm{T}}\mathbf{R}_x\mathbf{B}\mathbf{R}_x^{\mathrm{T}}\mathbf{R}_x\mathbf{c} = -\mathbf{e}_x^{\mathrm{T}}\mathbf{R}_x\mathbf{C}\mathbf{B}\mathbf{c}. \tag{13}$$

It can be easy to find that $\mathbf{e}_x^{\mathrm{T}}\mathbf{R}_x = \mathbf{e}_x^{\mathrm{T}}$. By substituting it in Equation (13), the x-axis component of the cross production can be rewritten

$$\mathbf{e}_x^{\mathrm{T}}\left[(\mathbf{b}' \times \mathbf{c}') \times \mathbf{c}'\right] = -\mathbf{e}_x^{\mathrm{T}}\mathbf{C}\mathbf{B}\mathbf{c} = \mathbf{e}_x^{\mathrm{T}}[(\mathbf{b} \times \mathbf{c}) \times \mathbf{c}]. \tag{14}$$

Furthermore, the x-axis component of the dot production can be derived as follows after rotation

$$\mathbf{e}_x^{\mathrm{T}}(\mathbf{b}'^{\mathrm{T}}\mathbf{c}')\mathbf{c}' = \mathbf{e}_x^{\mathrm{T}}\mathbf{R}_x\mathbf{c}(\mathbf{b}^{\mathrm{T}}\mathbf{R}_x^{\mathrm{T}}\mathbf{R}_x\mathbf{c}) = \mathbf{e}_x^{\mathrm{T}}(\mathbf{b}^{\mathrm{T}}\mathbf{c})\mathbf{c}. \tag{15}$$

If we assign the vectors $\mathbf{b} = \mathbf{e}_p$ and $\mathbf{c} = \mathbf{e}_{r_k}$, the conclusion can be drawn that the values w_{1k}^x and w_{2k}^x will not change when $\mathbf{e}_p$ and $\mathbf{e}_{r_k}$ being rotated θ along the x-axis, as illustrated in Figure 2. Without loss of generality, we can only calculate the spatial spectrum when $\phi = 0$ to reduce the computation burden. Thus, Equation (9) can be rewritten

$$P(\varphi,\, r_0,\, \mathbf{e}_p|\phi = 0) = \frac{1}{\mathbf{a}^{\mathrm{H}}\mathbf{P}_N\mathbf{a}}, \tag{16}$$

In this paper, our goal is to locate the electric sources, neglecting the source dipole moment $\mathbf{e}_p$. It is reasonable to hold the hypothesis that $\mathbf{e}_p$ has the same probability in each direction. Thus, we can rewrite Equation (16) as

$$P(\varphi, r_0) = P(\varphi, r_0 | \phi = 0, \mathbb{R}^3_{\mathbf{e}_p}) = \sum_{\mathbf{e}_p \in \mathbb{R}^3_{\mathbf{e}_p}} \frac{1}{\mathbf{a}^{\mathrm{H}} \mathbf{P}_N \mathbf{a}}. \tag{17}$$

where $\mathbb{R}^3_{\mathbf{e}_p}$ is a vector set that uniformly samples on the unit sphere. As a result, we can find the maximum values of $P(\varphi, r_0)$ in $\mathbb{R}^2$ space, not the $\mathbb{R}^6$ space in Equation (9), which reduces the calculation burden significantly.

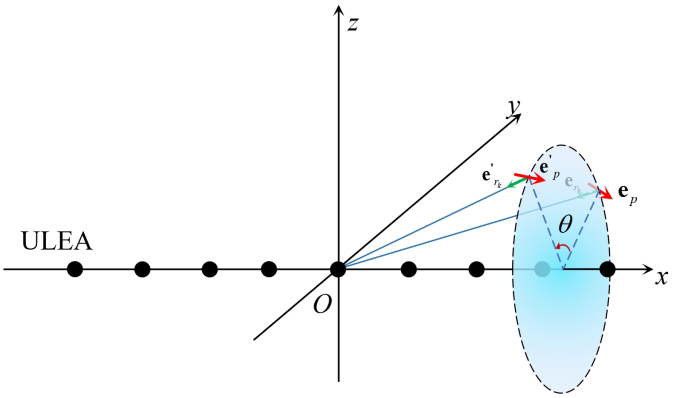

Figure 2. ULEA vector rotate model, where the vectors $\mathbf{e}_p$ and $\mathbf{e}_{r_k}$ are rotated θ along the x-axis.

Moreover, if we take deeper look at Equations (14) and (15) on the $x-y$ plane with $\phi = 0$, it can be easily derived that $\mathbf{e}_x^{\mathrm{T}}[(\mathbf{e}_z \times \mathbf{e}_{r_k}) \times \mathbf{e}_{r_k}] = 0$ and $\mathbf{e}_x^{\mathrm{T}}(\mathbf{e}_z^{\mathrm{T}} \mathbf{e}_{r_k}) \mathbf{e}_{r_k} = 0$. That means z-axis component of the dipole moment will have no contribution to the ULEA received signal. We can thereby further reduce the computation via sampling $\mathbf{e}_p$ uniformly on the unit circle of the $x-y$ plane, which is defined as a set $\mathbb{R}^2_{\mathbf{e}_p}$. Thus, Equation (17) can be rewritten as

$$P(\varphi, r_0) = P(\varphi, r_0 | \phi = 0, \mathbb{R}^2_{\mathbf{e}_p}) = \sum_{\mathbf{e}_p \in \mathbb{R}^2_{\mathbf{e}_p}} \frac{1}{\mathbf{a}^{\mathrm{H}} \mathbf{P}_N \mathbf{a}}. \tag{18}$$

In summary, the underwater electric sources locating method based on the ULEA is given by (Algorithm 1)

Algorithm 1: Underwater electric sources locating method based on ULEA

Data: The ULEA received signal $\mathbf{X}$

1 According to Equation (7), calculate the ensemble averaged covariance matrix $\mathbf{R}$. Subsequently, compute eigenvalues and eigenvectors from decomposition, which is $[\mathbf{V}, \mathbf{\Lambda}] = \mathrm{eigen}\{\mathbf{R}\}$;

2 Generate the noise subspace $\mathbf{V}_N$ based on the eigenvectors $\mathbf{V}$ and obtain the noise projection matrix $\mathbf{P}_N$ based on Equation (8);

3 Sample the point φ, r_0 in $\mathbb{R}^2$ space and generate the vector set $\mathbb{R}^2_{\mathbf{e}_p}$. Calculate the corresponding array manifold $\mathbf{a}$;

4 Obtain the spatial spectrum $P(\varphi, r_0)$ based on Equation (18);

5 Find the maximum values in $P(\varphi, r_0)$ and estimate the electric sources' locations $(\varphi_1, r_{01}), \cdots, (\varphi_D, r_{0D})$;

Result: locations $(\varphi_1, r_{01}), \cdots, (\varphi_D, r_{0D})$

3. Simulation

In this section, a ULEA of 21 voltage elements with the interval of 3 m is adopted in the simulation.

The electrical parameters of the water medium are specified as follows: the water conductivity is 3.5 S/m, and the relative permittivity and permeability are $\epsilon_r = 81.5$, $\mu_r = 1$, respectively, consistent with the properties of seawater. Two electric sources with a signal frequency of 2 kHz impinge onto the ULEA. Their positions are defined in the format $(\varphi,\ \phi,\ r_0,\ \mathbf{e}_p)$, which are $(120°, 0, 70, \left[\frac{1}{\sqrt{2}}, \frac{1}{\sqrt{2}}, 0\right]^{\mathrm{T}})$ and $(90°, 0, 73, \left[0, \frac{\sqrt{3}}{2}, \frac{1}{2}\right]^{\mathrm{T}})$. The corresponding dipole moment strengths are 10 A.m and 100 A.m, respectively. The localization algorithm is implemented on the MATLAB2018b platform. Figure 3 illustrates the electric field amplitude distribution of the two sources. It can be easily found that the field decays rapidly along their transmission paths.

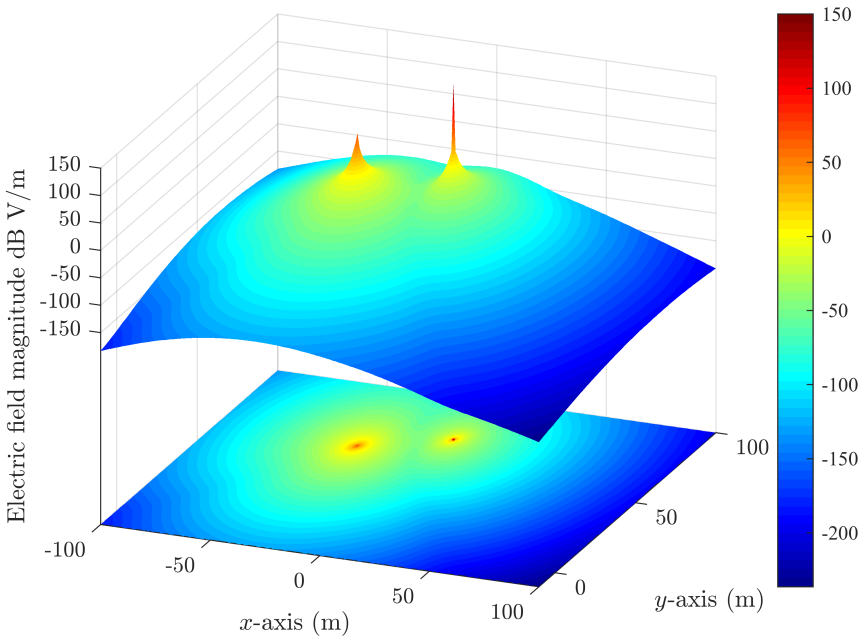

Figure 3. The synthetic electric field of two electric sources.

The signal received by ULEA is contaminated by uncorrelated AWGN. In this simulation, the signal-to-noise ratio (SNR) are set to 20 dB, 10 dB, and 6 dB with 600 snapshots collected. The spatial spectrum is computed with azimuth and distance intervals of 1° and 1 m, respectively. The simulation results are presented in Figure 4.

Figure 4a–c illustrate the estimation positions (φ, r_0) as follows: $(120°,\ 70)$, $(90°,\ 73)$ for SNR $=$ 20 dB; $(116°,\ 88)$, $(90°,\ 73)$ for SNR $=$ 10 dB and $(114°,\ 98)$, $(90°,\ 75)$ for SNR $=$ 6 dB. These results demonstrate satisfactory azimuth positioning accuracy. From the spatial spectrum slice in Figure 4d at $r_0 = 73$ m, the proposed MUSIC-based electric source positioning method exhibits sharp and distinct maximum values at azimuths 120° and 90° across the SNR range of 20∼6 dB. However, the intensity variation of the spatial spectrum within the range of 70∼80 m is only 1 dB when the SNR decreases to 6 dB for the source located at $(90°,\ 73)$. This minimal variation makes it challenging to accurately estimate the distance from ULEA to the sources, as shown in Figure 4e. The preliminary simulation results suggest that the proposed algorithm performs well in azimuth estimation but exhibits limited capability in distance estimation.

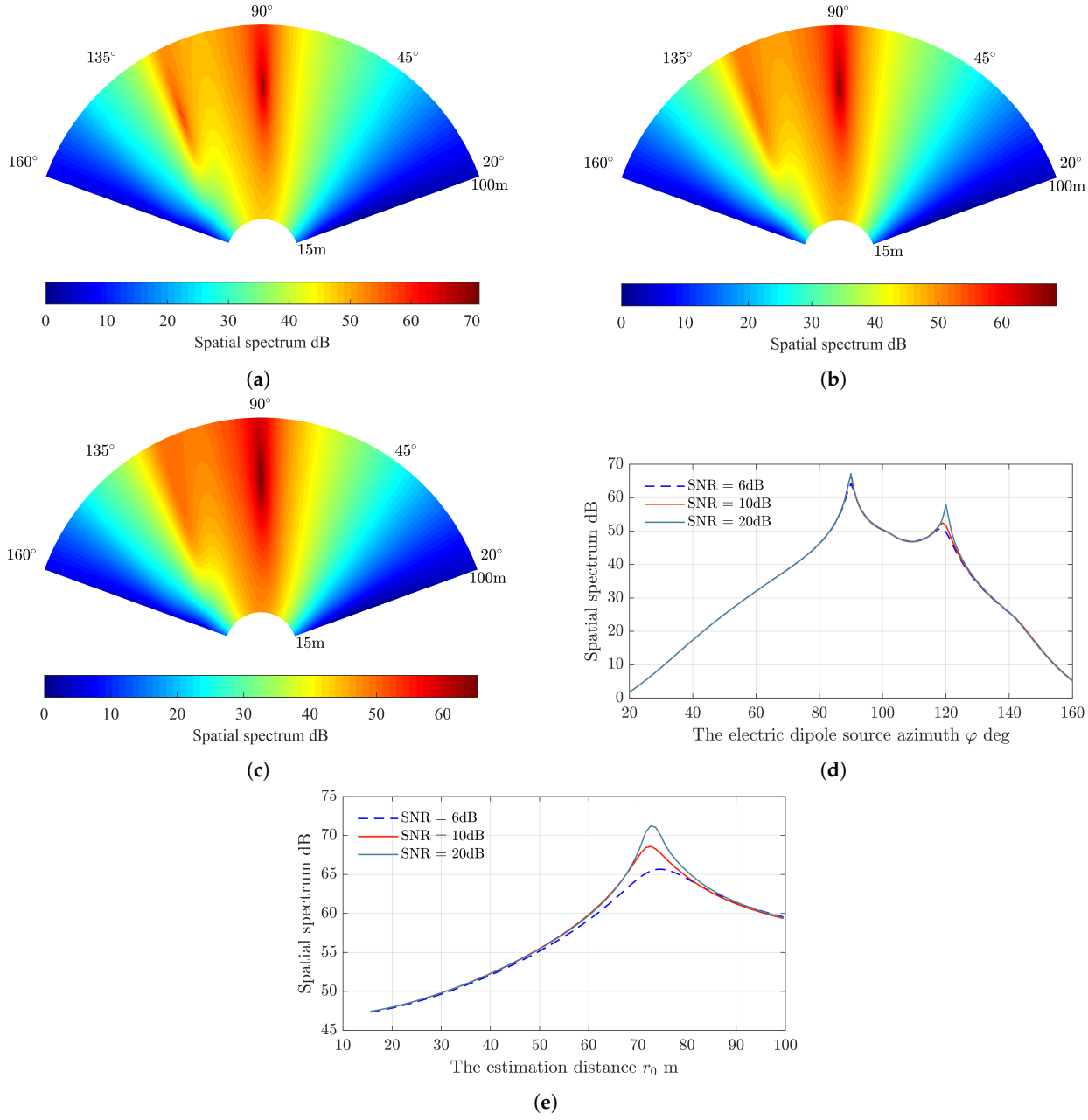

Figure 4. The spatial spectrum in range $\varphi \in (20°, 160°)$ and $r_0 \in (15, 100)$. (**a**) SNR = 20 dB. (**b**) SNR = 10 dB. (**c**) SNR = 6 dB. (**d**) The spatial spectrum slice when r_0 = 73 m. (**e**) The spatial spectrum slice when $\varphi = 90°$.

4. Performance Analysis

4.1. Resolution Analysis

In this subsection, the resolution performance of the MUSIC-based electric source localization method is discussed. In Benjamin Friedlander's work [27], a generalized resolution analysis method was proposed to distinguish two closely spaced signals in their parameter space. However, this method becomes highly complex when applied to scenarios involving more than two signals. For simplicity, we focus on a two-signal scenario, where the parameters are defined as $(\varphi_1, r_1 | \phi = 0, \mathbf{e}_p; \text{SNR}, N)$ and $(\varphi_2, r_2 | \phi = 0, \mathbf{e}_p; \text{SNR}, N)$. For the two signals to be distinguishable, the following condition must be satisfied:

$$\Delta E_i = E\{\hat{Z}(\varphi_0, r_0 | \phi = 0, \mathbf{e}_p; \text{SNR}, N)\} - E\{\hat{Z}(\varphi_i, r_i | \phi = 0, \mathbf{e}_p; \text{SNR}, N)\} \geq 0; \ i = 1, 2 \tag{19}$$

where $\hat{Z}(\varphi_i, r_i|\phi = 0, \mathbf{e}_p; \text{SNR}, N)$ represents the estimation of the zero spectrum $Z(\varphi_i, r_i|\phi = 0, \mathbf{e}_p; \text{SNR}, N)$. The zero spectrum is defined as $Z(\varphi_i, r_i|\phi = 0, \mathbf{e}_p; \text{SNR}, N) = \mathbf{a}^{\text{H}}\mathbf{P}_N\mathbf{a}$, where $i = 0, 1, 2$. Here, $Z(\cdot)$ is the reciprocal of spatial spectrum given in Equation (9). Additionally, we define $\varphi_0 = \frac{\varphi_1+\varphi_2}{2}$ and $r_0 = \frac{r_1+r_2}{2}$. To evaluate the resolution for different azimuth and distance values, the Monte Carlo method is employed, with each calculation performed 2000 times. Based on this, the corresponding azimuth resolution $\Delta\varphi$ is given by

$$\{\Delta\varphi = |\varphi_1 - \varphi_2| \, |\Delta E_i \geq 0; \; i = 1, 2\}, \tag{20}$$

the distance resolution Δr can be expressed as follows:

$$\{\Delta r = |r_1 - r_2| \, |\Delta E_i \geq 0; \; i = 1, 2\}. \tag{21}$$

In this simulation, the ULEA configuration remains consistent with that described in Section 3. We first evaluate the azimuth precision under varying SNR conditions, with the parameters specified as $(\varphi, 70|\phi = 0, [1, 0, 0]^{\text{T}}; \text{SNR}, 600)$. The results of the azimuth resolution are presented in Figure 5. Due to the symmetrical characteristics of the ULEA, the azimuth is evaluated within the interval $\varphi \in (20°, 90°)$. The corresponding resolutions for different azimuths are detailed in Table 1. The results demonstrate that the performance of the proposed localization method is related to the azimuth. Specifically, it provides satisfactory angle estimation when a parallel electric source is near the equatorial plane of the ULEA. Based on symmetry, we infer that the resolutions are less than 10° for $\varphi \in (70°, 110°)$ when the SNR $\geq$ 6 dB (indicated by the green area in the figure). However, the "blind spot" emerges for $\varphi \leq 50°$ and $\varphi \geq 130°$ (highlighted in the red area), where precision deteriorates significantly, particularly at lower SNR levels (e.g., SNR $\leq$ 10 dB).

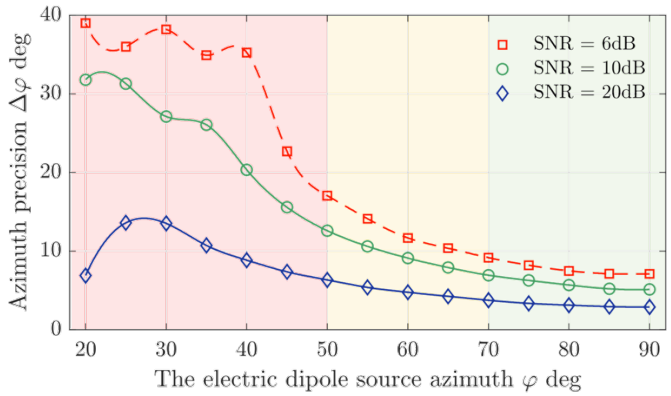

Figure 5. The azimuth precision with various SNR.

Table 1. The resolutions $\Delta\varphi$ of different azimuth φ.

Azimuth φ	$\Delta\varphi$ @ SNR = 6 dB	$\Delta\varphi$ @ SNR = 10 dB	$\Delta\varphi$ @ SNR = 20 dB
90°	7.11°	5.12°	2.89°
80°	7.48°	5.68°	3.12°
70°	9.16°	6.93°	3.75°
60°	11.67°	9.11°	4.76°
50°	17.04°	12.59°	6.33°
40°	35.26°	20.34°	8.84°
30°	38.23°	27.12°	13.52°
20°	39.01°	31.83°	6.88°

Figure 6 illustrates the spatial spectrum of two electric sources located at $(80^\circ + \frac{\Delta\varphi}{2}, 70\text{ m})$ and $(80^\circ - \frac{\Delta\varphi}{2}, 70\text{ m})$ for $\Delta\varphi = 5^\circ, 6^\circ, 8^\circ$ under an SNR condition of =10 dB. According to Table 1, the resolution at the point $(80^\circ, 70\text{ m})$ is 5.68°.

Figure 6 clearly demonstrates that when the two electric sources are too close (e.g., $\Delta\varphi = 5^\circ$, represented by the dark green dashed line), only a single spectrum peak is observed, making it impossible to distinguish the two sources. When the angular separation increases to 6°, which is slightly greater than the resolution of 5.68°, it becomes just possible to identify the presence of two sources. Finally, when the angular separation is $\Delta\varphi = 8^\circ$ (blue dashed line), two distinct spectrum peaks are clearly visible, illustrating that the two sources can be easily distinguished when the angular separation exceeds the resolution limit of 5.68°.

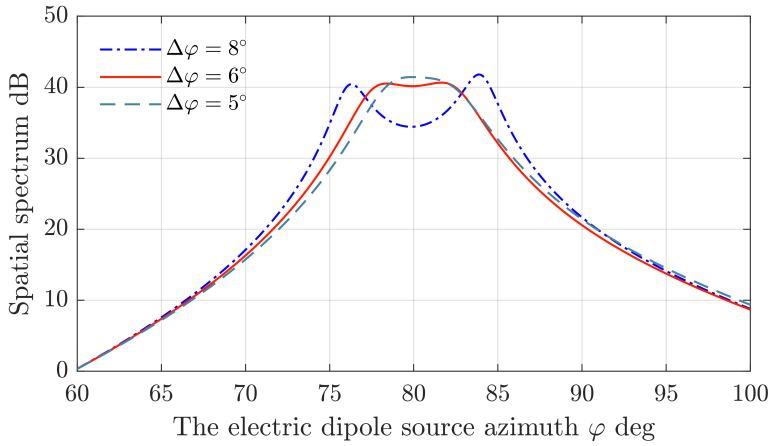

Figure 6. The spatial spectrum of two electric sources at parameter points $(80^\circ \pm \frac{\Delta\varphi}{2}, 70\text{ m})$ under the condition SNR = 10 dB.

The distance resolution Δr is also investigated. The parameters are set as $(90^\circ, r|\phi = 0, [1, 0, 0]^{\mathrm{T}}; 20\text{ dB}, 600)$. Based on our initial simulation, we observed that the localization algorithm struggles to distinguish between two sources with equivalent signal intensity. This difficulty arises due to the propagation characteristics of the electric field: the source closer to the ULEA generates a stronger voltage component compared to the one farther away. Table 2 presents the distance resolution results for an SNR of 20 dB. Two electric sources located 40 m away from the ULEA can be distinguished when their separation exceeds 11.6 m. As shown in Figure 7, the two sources cannot be resolved when they are too close (e.g., blue dashed line, $\Delta r = 10$ m). Furthermore, the distance resolutions Δr are on the same order of magnitude as the distances r themselves, indicating that the proposed algorithm is not well-suited for accurate distance estimation.

Table 2. The distance resolution of different r.

Distance r (Unit: m)	Resolution Δr (Unit: m)
10	3.4
15	5.3
20	6.7
25	8.0
30	9.2
35	10.4
40	11.5
45	14.4

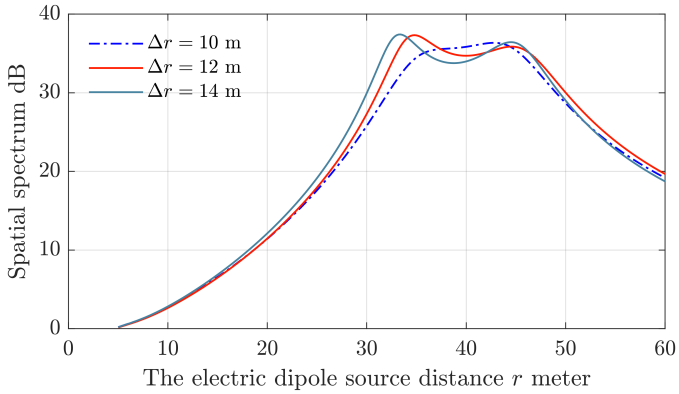

Figure 7. The spatial spectrum of two electric sources at parameter points $(90°, 40 \pm \frac{\Delta r}{2})$ under the condition SNR = 20 dB.

4.2. ULEA Structure & Locating Performance

According to the array manifold in Equation (5), the localization performance is strongly influenced by the ULEA structure, including the element number M, the sensor spacing Δl and the signal frequency f. In this subsection, we investigate the localization performance for different ULEA configurations by evaluating the precision defined in Equation (19) and the root mean square error (RMSE) of the azimuth estimation error.

Figure 8 presents simulation results comparing the localization performance for different numbers of elements M at the parameter points $(\varphi, 70\text{ m}|\phi = 0, [1, 0, 0]^{\mathrm{T}}; 20\text{ dB}, 600)$. It is evident that increasing the number of ULEA elements M enhances localization performance. However, this improvement comes at the cost of increased computational complexity and a more complex array manifold $\mathbf{a}$, as defined in Equation (4). Notably, the performance gain diminishes significantly when M exceeds 25. For example, when M increases from 13 to 17 at an azimuth of $\varphi = 90°$, the resolution improves from 3.85° to 3.24°, a gain of 0.62°. In contrast, when M increases from 25 to 29, the resolution only improves from 2.59° to 2.55°, a marginal gain of 0.04°. Therefore, the choice of M should be carefully balanced between computational burden and the desired resolution improvement.

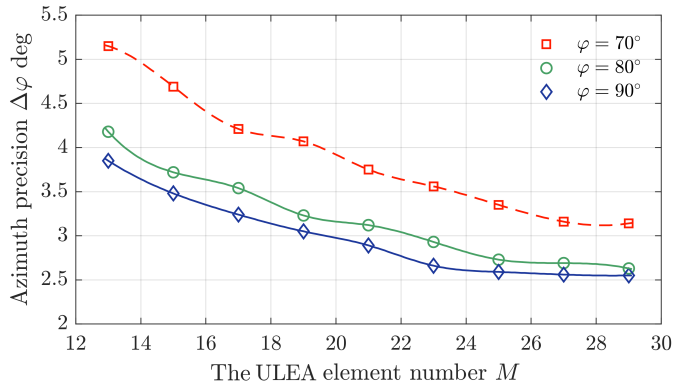

Figure 8. The azimuth precision with various ULEA element number M when the SNR is 20 dB.

In Figure 9, the RMSE of the azimuth estimation for a single electric source is illustrated. In this simulation, the target is positioned at parameter points $(\varphi, 70\text{ m}|\phi = 0, [1, 0, 0]^{\mathrm{T}}; \mathrm{SNR}, 600)$, where $\varphi = 70°, 80°, 90°$; and the SNR values are set to 20 dB, 10 dB, and 6 dB. The results demonstrate that both increasing the SNR and the number of elements M can effectively reduce the azimuth estimation error. However, similar to previous findings, the improvement becomes negligible when M exceeds 25. As shown in Figure 9, even under the worst-case scenario in this comparison, the azimuth error remains below 0.16° for an SNR of 6 dB with only 13 ULEA sensor elements. This indicates that the

proposed localization algorithm delivers satisfactory azimuth estimation performance for single-target scenarios.

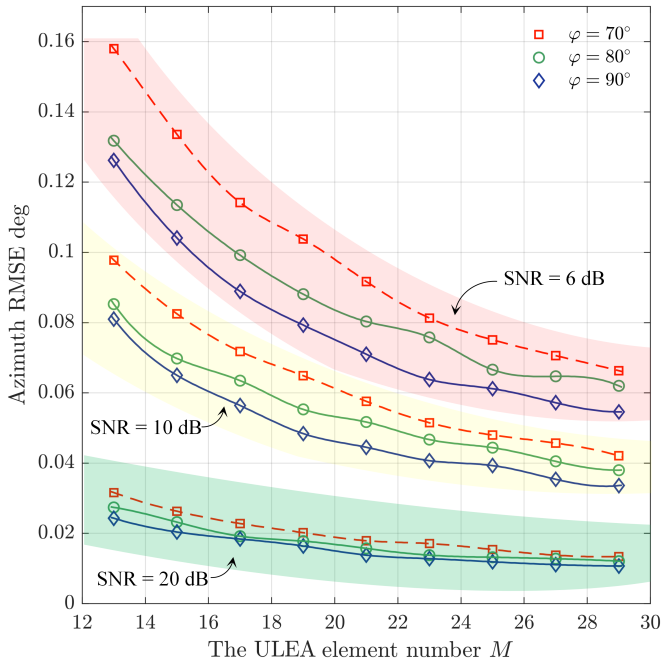

Figure 9. The azimuth estimation's RMSE with various ULEA voltage sensor number M.

In canonical array signal processing applications, the array element spacing Δl defines the array aperture. In this paper, Δl plays a similar role, as it is closely related to the array manifold. We investigate the azimuth resolution by setting the parameters $(90°, 70\text{ m}|\phi = 0, [1, 0, 0]^{\mathrm{T}}; 20\text{ dB}, 600)$ with the ULEA voltage sensor number $M = 21$. As shown in Figure 10, the simulation result demonstrates the resolution significantly improves from 13.24° to 2.71° as Δl increases from 0.5 m to 5 m. The resolution of the localization algorithm stabilizes around 2.60°. However, due to the propagation path, the signal strength received by voltage sensors far from the target becomes significantly weaker compared to those closer to it, resulting in a loss of positioning capability. Consequently, the azimuth resolution performance degrades when Δl is further increased (e.g., $\Delta l \geq 30$). The corresponding spatial spectra are illustrated in Figure 11. The left column of the figure shows scenarios where the angular separation is below the azimuth resolution, making the targets indistinguishable. In contrast, the right column depicts scenarios where the angular separation exceeds the resolution, allowing for clear distinction between targets.

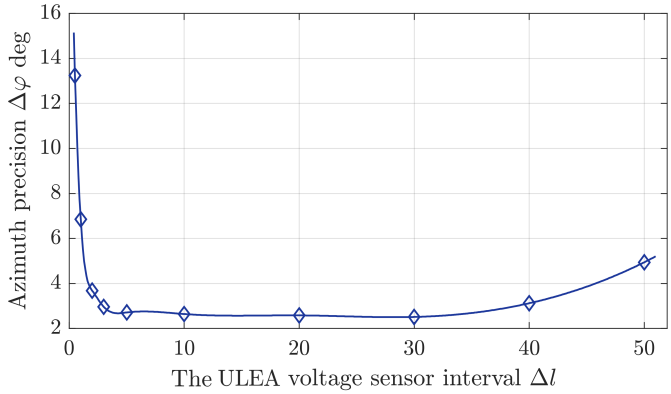

Figure 10. The azimuth precision with various ULEA voltage sensor element interval Δl.

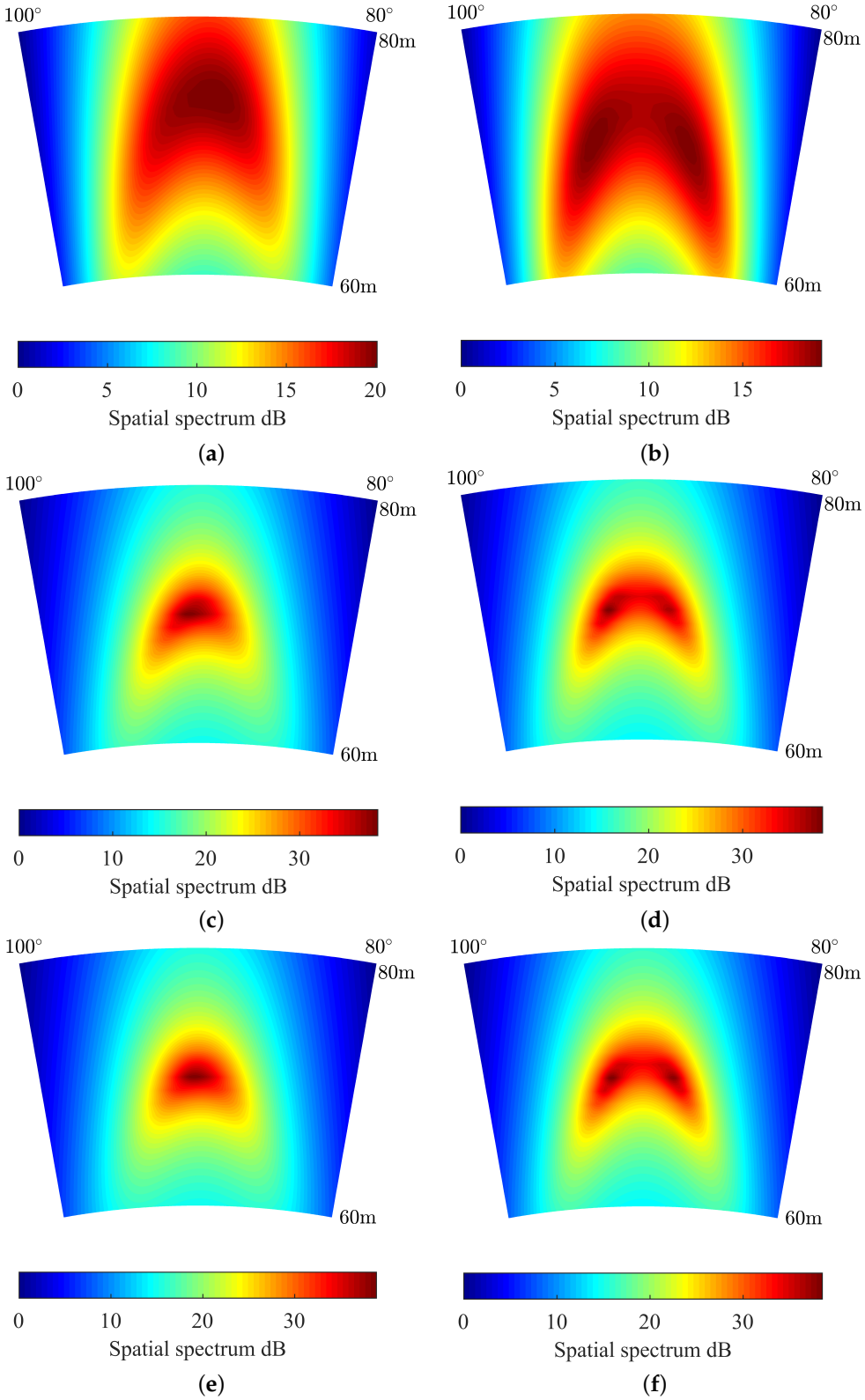

Figure 11. The spatial spectrum in range $\varphi \in (80°, 100°)$. (**a**) The simulation settings $\Delta l = 1$, the azimuth difference is 6°. (**b**) The simulation settings $\Delta l = 1$, the azimuth difference of the two electric sources is 8°. (**c**) The simulation settings $\Delta l = 5$, the azimuth difference is 2°. (**d**) The simulation settings $\Delta l = 5$, the azimuth difference is 4°. (**e**) The simulation settings $\Delta l = 10$, the azimuth difference is 2°. (**f**) The simulation settings $\Delta l = 10$, the azimuth difference is 4°.

We employ the same parameter configuration as above to evaluate the RMSE of azimuth estimation under a single electric source condition, as illustrated in Figure 12.

The localization performance is significantly improved by increasing the array element spacing within the range of $\Delta l \in (0, 5)$. Subsequently, the RMSE stabilizes at 0.01° when $\Delta l \in (5, 40)$. However, the locating performance degrades as continuously increasing Δl. Through comprehensive analysis of both resolution and the RMSE of azimuth estimation, we conclude that the proposed localization method exhibits a characteristic "frying pan" pattern in relation to Δl. This pattern provides valuable guidance for minimizing the ULEA size while maintaining the required precision and localization accuracy. Based on our findings, we recommend an optimal ULEA size corresponding to the Δl value at the left side "L" corner in either Figure 10 or Figure 12, specifically at $\Delta l = 3$. This configuration optimally balances localization performance with ULEA size efficiency.

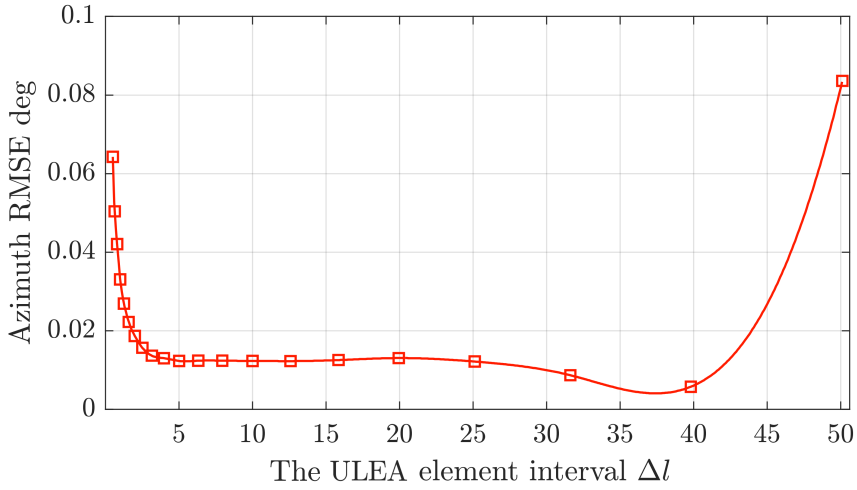

Figure 12. The azimuth estimation's RMSE with various ULEA element interval Δl when the SNR is 20 dB.

5. Conclusions

In this paper, we propose a MUSIC-based localization method utilizing a ULEA for underwater electric sources. The electric field component along the axis of the ULEA is employed to construct the array manifold, which not only simplifies the theoretical framework but also facilitates practical deployment. By leveraging the symmetry and rotational invariance of the ULEA, the computational complexity of calculating the spatial spectrum is significantly reduced from $\mathbb{R}^6_{\mathbf{e}_p}$ to $\mathbb{R}^2_{\mathbf{e}_p}$. Our analysis demonstrates that the proposed method achieves satisfactory azimuth discrimination performance within the specific angular range of 50° to 130°, with an azimuth resolution of up to 2.89°. However, blind zones emerge outside this interval, limiting the method's effectiveness in those regions. Furthermore, the method demonstrated would reduce positioning accuracy for electric sources located within 10 m of the ULEA. The structure of the ULEA, particularly the number of voltage sensors M and their spacing Δl, plays a critical role in determining the array manifold, the azimuth precision and error. Increasing the number of sensors (up to $M \leq 25$) can significantly improve the localization performance. On the other hand, varying the sensor interval Δl reveals a characteristic "frying pan" pattern in localization performance. Based on this observation, we recommend an optimal compromise value of $\Delta l = 5$, which balances localization accuracy with ULEA size efficiency. In future work, we aim to implement and validate the proposed localization system in an experimental environment, further refining its performance and applicability in real-world scenarios.

Author Contributions: Conceptualization, W.S. and Y.X.; methodology, W.S., Y.X. and V.M.O.; validation, F.G. and Y.P.; data analysis, J.L., F.G. and Y.P.; writing—original draft preparation, W.S., J.L. and Y.X.; writing—review and editing, W.S., S.V.V. and V.M.O.; visualization, J.L., F.G. and Y.P.; supervision, W.S. and Y.X.; project administration, Y.X.; funding acquisition, Y.X. All authors have reviewed and consented to the final version of the manuscript for publication.

Funding: This work was supported by Ye Qisun Science Foundation of National Natural Science Foundation of China (Grant No. U2441288), the National Natural Science Foundation of China (No. 52101383), the Fundamental Research Funds for the Central Universities (No. 3072024JJ2702) and the Ministry of Science and Higher Education of the Russian Federation as part of the World-class Research Center program: Advanced Digital Technologies (contract No. 075-15-2022-311 dated 20 April 2022).

Institutional Review Board Statement: Not applicable.

Informed Consent Statement: Not applicable.

Data Availability Statement: The data featured in this study can be obtained upon request from the corresponding author.

Conflicts of Interest: The authors declare no conflicts of interest.

References

1. Park, D.; Kwak, K.; Kim, J.; Chung, W.K. Underwater sensor network using received signal strength of electromagnetic waves. In Proceedings of the 2015 IEEE/RSJ International Conference on Intelligent Robots and Systems (IROS), Hamburg, Germany, 28 September–2 October 2015; pp. 1052–1057.
2. Quintana-Diaz, G.; Mena-Rodriguez, P.; Perez-Alvarez, I.; Jimenez, E.; Dorta-Naranjo, B.P.; Zazo, S.; Perez, M.; Quevedo, E.; Cardona, L.; Joaquin Hernandez, J. Underwater Electromagnetic Sensor Networks-Part I: Link Characterization. *Sensors* **2017**, *17*, 189. [CrossRef] [PubMed]
3. Kim, J.H.; Jeon, J.C.; Yoo, J.G. The Measurement for the Underwater Electric Field Using a Underwater 3-Axis Electric Potential Sensor. In Proceedings of the International Conference on Grid and Distributed Computing, Jeju Island, Republic of Korea, 8–10 December 2011; pp. 408–414.
4. Zhenbin, Z.; Bin, L. Underwater Electromagnetic Sources 2-D DOA and Polarization Estimation. In Proceedings of the 2012 Second International Conference on Industry, Information System and Material Engineering (IISME 2012), Wuhan, China, 17–18 March 2012; pp. 529–534.
5. Boyer, F.; Lebastard, V.; Ferrer, S.B.; Geffard, F. Underwater pre-touch based on artificial electric sense. *Int. J. Robot. Res.* **2020**, *39*, 729–752. [CrossRef]
6. Boyer, F.; Lebastard, V.; Chevallereau, C.; Mintchev, S.; Stefanini, C. Underwater navigation based on passive electric sense: New perspectives for underwater docking. *Int. J. Robot. Res.* **2015**, *34*, 1228–1250. [CrossRef]
7. Zheng, J.; Wang, J.; Guo, X.; Huntrakul, C.; Wang, C.; Xie, G. Biomimetic Electric Sense-Based Localization: A Solution for Small Underwater Robots in a Large-Scale Environment. *IEEE Robot. Autom. Mag.* **2022**, *29*, 50–65. [CrossRef]
8. Zhao, Z.; Hu, Q.; Feng, H.; Feng, X.; Su, W. A Cooperative Hunting Method for Multi-AUV Swarm in Underwater Weak Information Environment with Obstacles. *J. Mar. Sci. Eng.* **2022**, *10*, 1266. [CrossRef]
9. Nguyen, N.; Wiegand, I.; Jones, D.L. Sparse Beamforming for Active Underwater Electrolocation. In Proceedings of the 2009 IEEE International Conference on Acoustics, Speech, and Signal Processing (ICASSP), Taipei, Taiwan, 19–24 April 2009; Volumes 1–8, pp. 2033–2036.
10. Lim, H.S.; Ng, B.P.; Reddy, V.V. Generalized MUSIC-Like Array Processing for Underwater Environments. *IEEE J. Ocean. Eng.* **2017**, *42*, 124–134. [CrossRef]
11. Lanneau, S.; Boyer, F.; Lebastard, V.; Bazeille, S. Model based estimation of ellipsoidal object using artificial electric sense. *Int. J. Robot. Res.* **2017**, *36*, 1022–1041. [CrossRef]
12. Shang, W.; Xue, W.; Li, Y.; Wu, X.; Xu, Y. An Improved Underwater Electric Field-Based Target Localization Combining Subspace Scanning Algorithm And Meta-EP PSO Algorithm. *J. Mar. Sci. Eng.* **2020**, *8*, 232. [CrossRef]
13. Yang, M.; Ding, J.; Chen, B.; Yuan, X. A Multiscale Sparse Array of Spatially Spread Electromagnetic-Vector-Sensors for Direction Finding and Polarization Estimation. *IEEE Access* **2018**, *6*, 9807–9818. [CrossRef]
14. Schmidt, S.O.; John, F.; Hellbrueck, H. Evaluation of 3-dimensional Electrical Impedance Tomography-Arrays for Underwater Object Detection. In Proceedings of the OCEANS 2022, Chennai, India, 21–24 February 2022.

15. Kim, J.; Son-Cheol, Y.; Bae, K.W. Calibrating Electrode Misplacement in Underwater Electric Field Sensor Arrays for the Electric Field-Based Localization of Underwater Vessels. *J. Sens. Sci. Technol.* **2022**, *31*, 330–336. [CrossRef]
16. Wang, C.; Xu, Y.; Qi, J.; Shang, W.; Liu, M.; Chen, W. Passive Electromagnetic Field Positioning Method Based on BP Neural Network in Underwater 3-D Space. In Proceedings of the 5th EAI International Conference of Advanced Hybrid Information Processing (ADHIP 2021), Virtual Event, 22–24 October 2021; pp. 292–304.
17. Liu, Z.; Gao, J.; Xu, L.; Jia, P.; Pan, D.; Xue, W. Electromagnetic Fusion Underwater Positioning Technology Based on ElasticNet Regression Method. In Proceedings of the 2022 IEEE 10th International Conference on Information, Communication and Networks (ICICN 2022), Zhangye, China, 23–24 August 2022; pp. 121–126.
18. Peng, J.; Wu, J. A Numerical Simulation Model of the Induce Polarization: Ideal Electric Field Coupling System for Underwater Active Electrolocation Method. *IEEE Trans. Appl. Supercond.* **2016**, *26*, 0606305. [CrossRef]
19. Peng, J.; Zhu, Y.; Yong, T. Research on Location Characteristics and Algorithms based on Frequency Domain for a 2D Underwater Active Electrolocation Positioning System. *J. Bionic Eng.* **2017**, *14*, 759–769. [CrossRef]
20. Ren, Q.; Peng, J.; Chen, H. Amplitude information-frequency characteristics for multi-frequency excitation of underwater active electrolocation systems. *Bioinspiration Biomim.* **2020**, *15*, 016004. [CrossRef] [PubMed]
21. Han, Y.; Wu, H.; Peng, J.; Ou, B. The Effect of Object Geometric Features on Frequency Inflection Point of Underwater Active Electrolocation System. *J. Mar. Sci. Eng.* **2021**, *9*, 756. [CrossRef]
22. Liu, Y.; Hu, Q.; Yang, Q.; Li, Y.; Fu, T. An underwater moving dipole tracking method of artificial lateral line based on intelligent optimization and recursive filter. *Meas. Sci. Technol.* **2022**, *33*, 075113. [CrossRef]
23. Peng, H.; Jiang, G.; Hu, Q.; Fu, T.; Xu, D. Locating and tracking of underwater sphere target based on active electrosense. *Sens. Actuators Phys.* **2023**, *363*, 114671. [CrossRef]
24. Li, S.; Hu, Q.; Yang, Q.; Fu, T. Tracking the Underwater Moving Dipole with the Artificial Lateral Line Based on the PAST and KF. In Proceedings of the 2022 International Conference on Autonomous Unmanned Systems, ICAUS 2022, Xi'an, China, 23–25 September 2022; Lecture Notes in Electrical Engineering; Volume 1010, pp. 223–232.
25. Wang, X.; Wang, S.; Hu, Y.; Tong, Y. Mixed electric field of multi-shaft ship based on oxygen mass transfer process under turbulent conditions. *Electronics* **2022**, *11*, 3684. [CrossRef]
26. Kraichman, M.B. *Handbook of Electromagnetic Propagation in Conducting Media*; Headquarters Naval Material Command: Mechanicsburg, PA, USA, 1976.
27. Friedlander, B.; Weiss, A.J. The resolution threshold of a direction-finding algorithm for diversely polarized arrays. *IEEE Trans. Signal Process.* **1994**, *42*, 1719–1727. [CrossRef]